Supplementary Information

Stretchable Polymeric-Gel-Based Sponge with Tunable Wettability via Segmented Network Design

Hyebhin Yoon,[a,b] Ju Hyeon Kim,[a] Jongmin Q. Kim,[a] Jin Woo Bae,[c,] Eun-Ho Sohn,[a,*] and Hong Suk Kang [d,*]*

[a] Interface Material and Chemical Engineering Research Center, Korea Research Institute of Chemical Technology, 141 Gajeong-ro, Yuseong-gu, Daejeon 34114, Republic of Korea
[b] School of Chemical and Biological Engineering, and Institute of Chemical Processes, Seoul National University, 1 Gwanak-ro, Gwanak-gu, Seoul 08826, Republic of Korea
[c] Multifunctional Organic Polymer Laboratory, Future Convergence Engineering, School of Energy, Materials and Chemical Engineering, Korea University of Technology and Education, 1600 Chungjeol-ro, Cheonan 31253, Republic of Korea
[d] Department of Polymer Science and Engineering and Program in Environmental and Polymer Engineering, Inha University, Incheon 22212, Republic of Korea

Corresponding Author

E-mail (Prof. Jin Woo Bae): jwbae@koreatech.ac.kr

E-mail (Dr. Eun-Ho Sohn): inseh98@krict.re.kr

E-mail (Prof. Hong Suk Kang): hskang@inha.ac.kr

Table of contents

List of figures

List of tables

List of supplementary movies

Movie S3. PGM-HFBA sponge absorbing silicon oil.

Movie S4. PGM-HFBA sponge absorbing only silicon oil from mixture of oil and water.

Movie S5. PGM-HFBA sponge releasing silicone oil by 2 N force.

Movie S6. PGM-HFBA sponge releasing silicone oil by hand squeezing.

Movie S7. Electronic conductive, liquid metal-absorbing PGM-HEA sponge under stretching.

Movie S8. Electronic conductive liquid metal-absorbing PGM-HEA sponge under twisting.

Movie S9. Electronic conductive liquid metal-absorbing PGM-HEA sponge attached to a finger joint.

Detailed information of experiments

Calculation of gel contents and swelling rate of the polymeric gel

At first, the synthesized polymeric gel was cut to 10 mm × 10 mm square centimeter, and the weight of each film was measured (initial weight, m_0). Next the each cut film was put into 50 mL vial, and poured 30 g of THF into vial with stirring at 300 RPM for 24 hours. After 24 hours, the swelled film was obtained, and measured the film`s weight (swelled weight, m_1). Next, the swelled film was dried in a vacuum oven at 60 °C for 24 hours, and the weight was measured (re-dried weight, m_2). Gel contents were calculated as follows:

$$Gel\ content\ (\%) = \frac{m_2}{m_0} \times 100$$

And swelling rates were calculated using following equation:

$$Swelling\ rate\ (\%) = \frac{(m_1 - m_0)}{m_0} \times 100$$

Calculation of statistical error

Observation of statistical error was performed through collecting 10–20 of data points and calculating each average and deviation. Average and standard deviation were calculated using equations as follows:

$$Average\ (\mu) = \frac{1}{N}\sum_{i=1}^{N} x_i$$

$$Standard\ deviation\ (\sigma) = \sqrt{\frac{1}{N}\sum_{i=1}^{N}(x_i - \mu)^2}$$

where x_i is each data value for number i.

Estimation of the surface free energy

To estimation the surface free energy (γ_s) of material using Owens–Wendt–Rabel–Kaelble (OWRK) method, two independent equations based on contact angles with two different liquids are required. The Young's equation applied in this context is:

$$\gamma_{L,i}(1 + \cos\theta_i) = 2(\sqrt{\gamma_s^d \gamma_{L,i}^d} + \sqrt{\gamma_s^p \gamma_{L,i}^p})$$

where $\gamma_{L,i}$ is the surface tension of liquid *i*, θ_i is contact angle with liquid *i*, γ_s is the surface free energy of the solid, γ^d and γ^p represent the dispersion and polar component. Especially, γ_s^d and γ_s^p indicate the dispersion and polar component of solid, $\gamma_{L,i}^d$ and $\gamma_{L,i}^p$ indicate the dispersion

and polar component of contacted liquid. [1-3] And total surface free energy is then given by:

$\gamma = \gamma^d + \gamma^p$

In this study, the contact angles between the polymeric gel material (PGM) and water (θ_{water}) or hexadecane (θ_{HD}) were measured using the sessile drop under 25 °C and RH 40%. Accordingly, two separate equations of water and hexadecane can be formulated based on the measured contact angles. At first, the equation for water is as follows:

$72.8(1 + \cos\theta_{water}) = 2(\sqrt{\gamma_s^d \times 22.1} + \sqrt{\gamma_s^p \times 50.7})$

Here, the surface tension of water ($\gamma_{L,\,water}$), is 72.8 mN/m, with a dispersion component (γ_{water}^{d}) of 22.1 mN/m and a polar component (γ_{water}^{p}) of 50.7 mN/m. And these values were obtained from *HANDBOOK OF Applied Surface and Colloid Chemistry*. [4]

In addition, another equation for hexadecane is given by:

$27.3(1 + \cos\theta_{HD}) = 2(\sqrt{\gamma_s^d \times 27.3} + \sqrt{\gamma_s^p \times 0})$

where, the surface tension of hexadecane ($\gamma_{L,\,HD}$) is 27.3 mN/m, consisting entirely of a dispersion component (γ_{HD}^{d}), with a negligible polar component (γ_{HD}^{p}). These values were also collected from *HANDBOOK OF Applied Surface and Colloid Chemistry*. [4] Especially, the polar component of hexadecane was considered to be zero, since it is a non-polar organic compound. [2] Similarly, diiodomethane, a representative non-polar organic compounds, also exhibits a near-zero polar component (γ^p), according to *HANDBOOK OF Surface and Colloid Chemistry*. [5] Therefore, the dispersion component of non-polar hexadecane was calculated as 27.3. These two independent equations are appropriate to calculate the dispersive (γ_s^d) and polar (γ_s^p) component of PGMs. Therefore, the surface free energy of PGMs was calculated by combining two components: γ_s^d and γ_s^p.

Preparation for the sacrificial salt frame

NaCl microparticles were ground using a ball mill with stainless steel balls for varying durations of 10 minutes, 30 minutes, 1 hour, and 3 hours to control the particle size. After ball milling, the sacrificial salt frame was prepared as follows: the ground NaCl (10 g) was mixed thoroughly with deionized (DI) water (2 g) to form a high-viscosity slurry. This slurry was poured onto a Teflon plate and dried in a vacuum oven at 80 °C for 48 hours. After drying, the sacrificial NaCl frame was carefully removed from the Teflon plate for subsequent use.

Evaluation of water/oil separation properties of PGM-HFBA sponge

For applying water/oil separation field, evaluation of PGM-HFBA sponge was conducted. The precise difference between separation efficiency and absorption capacity is how much absorbs oil from water/oil mixture or only oil phase. In addition, the silicon oil (Dow Corning, 500 mL) was employed, and dyed to red color using oil red O (Sigma Aldrich, 25 g) for ease of visual observation. First, the separation efficiency was calculated as follows:

$$Separation\ efficiency\ (\%) = \frac{(m_2 - m_0)}{(m_1 - m_0)} \times 100$$

, where m_0 is initial weight of sponge, m_1 is oil absorbed weight from water/oil mixture, and m_2 is water-dried weight of sponge (dry condition: 80℃, 90 minutes). On the other hand, Absorption capacity was calculated applying following equation:

$$Absorption\ capacity\ (\%) = \frac{(m_1 - m_0)}{m_0} \times 100$$

, where m_0 is initial weight, and m_1 is sponge weight after absorbing oil. The m_0 term indicates the weight of clean and uncontaminated sponge before any absorption test. In addition, the recovery rate was calculated according to the types of liquids as follows:

$$Recovery\ rate\ (\%) = \frac{(m_1 - m_2)}{(m_1 - m_0)} \times 100$$

, where m_0 is initial weight, m_1 is oil absorbed sponge weight, and m_2 is squeezed sponge weigh after absorbing oil. The denominator term means the ideal oil weight obtained by absorbing, and the numerator term indicates the real oil weight that collected from squeezing. Recovery rate should be under 100% derived by the remained oil despite squeezing, due to the low surface energy interaction between oil and PGM-HFBA sponge.

The taping test was performed by repeating attaching and detaching of scotch tape (3M) from the surface of sponge, and the water contact angle was recorded every 50 cycles. Besides, scrub test was operated applying friction to the sponge with a sandpaper (120 grit). Likewise, the water contact angle was measured every 50 cycles.

Preparation for the liquid metal absorbed sponge

Liquid metal (LM)-absorbed sponge was prepared by penetrating Gallium-Indium eutectic (Sigma Aldrich, 5 g) to the PGM-HEA hydrophilic sponge. For the ease of penetration, poured LM to the surface of PGM-HEA sponge, and put into the vacuum oven for 24 hours. After 24 hours, the LM-absorbed sponge was taken out from the LM.

Preparation for an encapsulated stretchable conductor

For fabrication of a strain conductor, as-prepared LM-absorbed sponge and transparent PGM film were combined by sandwiching them. The first layer was PGM film, and put LM-absorbed sponge on it. Then one leg of each two LED lamps were connected to inside of the LM-absorbed sponge, and other sides were connected to a battery (Bexel, 9V). Finally, stretchable polymeric gel covered the sponge as a third layer.

Characterization

FT-IR spectroscopy was performed using a Nicolet 5700 spectrometer. Differential scanning calorimetry (DSC) and thermogravimetric analysis (TGA) were carried out using DSC Q1000 and TGA Q5000 instruments, respectively, both manufactured by TA Instruments. Surface chemical compositions were analyzed using X-ray photoelectron spectroscopy (XPS) with a Nexsa G2 instrument (Thermo Scientific).

Discussion on the chemical compatibility of materials

For evaluation the miscibility of the chemicals in this study, we considered their solubility parameters. As shown in **Figure S1**, ethyl acrylate (EA), poly(ethylene glycol) dimethacrylate (PEGDMA), 2-hydroxyethyl acrylate (HEA), and 2,2,3,4,4,4-hexafluorobutyl acrylate has a solubility parameter of 18.1 $MPa^{0.5}$,19.4 $MPa^{0.5}$, 22.0 $MPa^{0.5}$, and 15.2 $MPa^{0.5}$, respectively. At first, as the solubility parameter differences among EA, PEGDMA, and HEA are less than 5 $MPa^{0.5}$, the mentioned chemicals are considered mutually miscible. In addition, the solubility parameter differences below 5 $MPa^{0.5}$ among EA, PEGDMA, and HFBA are recognized miscible. This miscibility enables the homogenous mixture, and formation of a homogenous crosslinked polymer structure, supporting stable and uniform wettability control throughout the PGM.

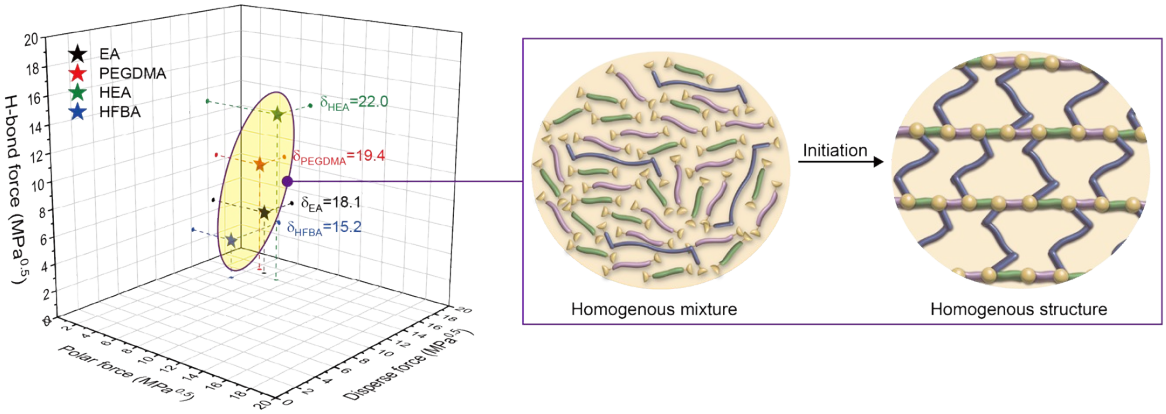

Figure S1. Solubility parameter calculated from polar force, disperse force, H-bond force of EA, PEGDMA, HEA, and HFBA (right) and their illustration (left).

Discussion on chemical structure of PGM

As shown in **Figure S2**, the successful polymerization of PGM was clearly confirmed. Specifically, characteristic peaks corresponding to key functional groups were observed, including C-H stretching for alkanes (3023–2761 cm^{-1}), C=O stretching for esters (1724 cm^{-1}), C=C stretching (1633 cm^{-1}), -CH_3 bending (1448 cm^{-1}), C-O stretching for esters (1155 cm^{-1}), and C=C bending (985 cm^{-1}). Notably, the C=C stretching peak of PGM was significantly reduced compared to that of EA, indicating the successful polymerization process.

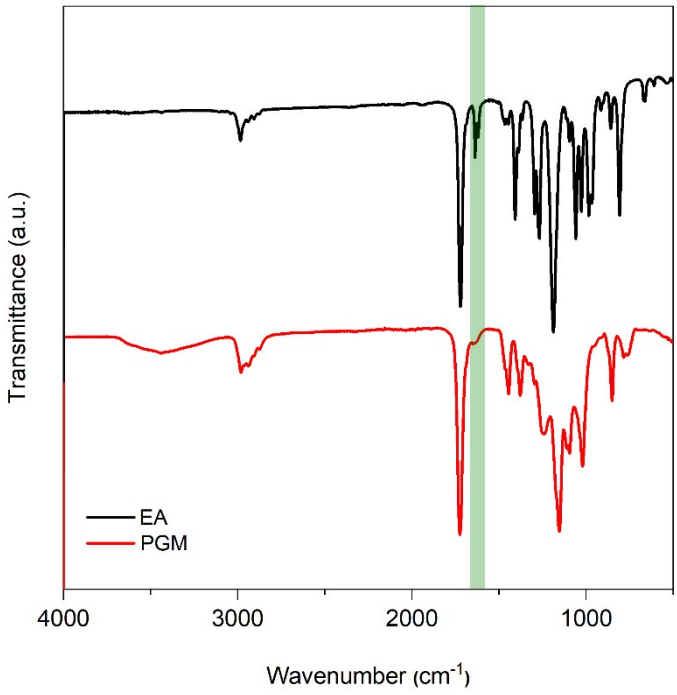

Figure S2. FT-IR spectrum of ethyl acrylate (black) and PGM (red).

Discussion on the thermogravimetric properties of PGM

As shown in **Figure S3**, DSC and TGA analyses were conducted to evaluate the crosslinking characteristics of PGM. According to **Figure S3a**, the glass transition temperature (T_g) of PGM increased from -21.7 °C (non-crosslinked) to -14.6 °C (crosslinked). This increase is attributed to the tightly crosslinked network, which restricts polymer chain mobility, requiring more energy for segmental motion and consequently resulting in a higher T_g.[6]

Furthermore, thermogravimetric analysis (TGA) in **Figure S3b** confirmed the thermal stability of PGM. The temperature at which 1 wt% mass loss occurred was significantly higher for crosslinked PGM (256.7 °C) compared to the non-crosslinked counterpart (132.9 °C). This enhanced thermal stability further supports the formation of a robust crosslinked structure within PGM.

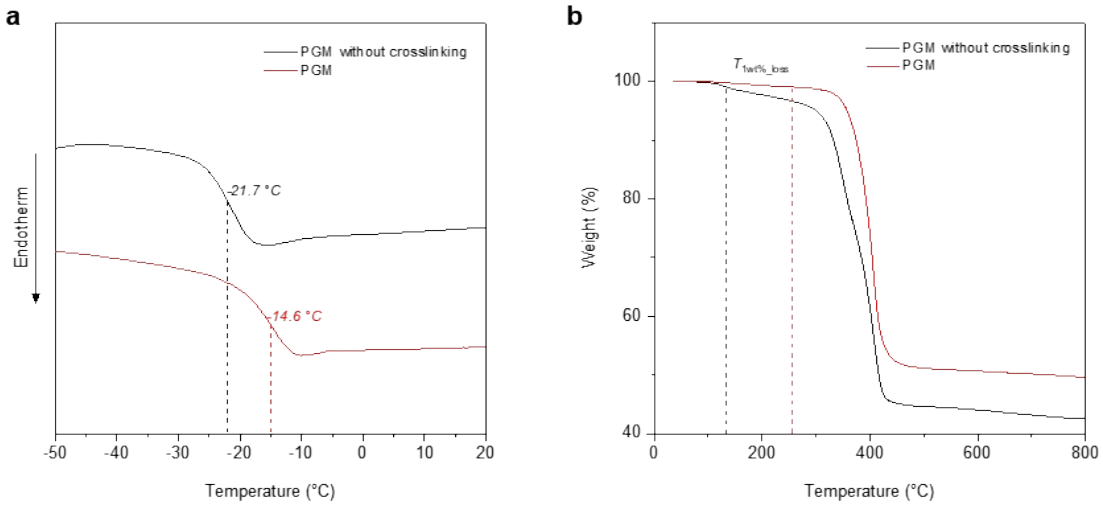

Figure S3. (a) DSC and (b) TGA analysis of PGM without crosslinking (black) and PGM (red).

Discussion on the X-ray photoelectron spectroscopy (XPS) of PGMs

As shown in **Figure S4**, the XPS analysis of PGM, PGM-HFBA, and PGM-HEA confirms the successful incorporation of functional moieties. **Figure S4a** clearly displays the fluorine 1s peak, which originates from the presence of HFBA, indicating the successful integration of fluorinated groups into the polymer matrix. Meanwhile, PGM-HEA exhibited a higher oxygen content than PGM, as demonstrated in **Figures S4b–c**. Specifically, the O-H bonding from HEA was distinctly observed through the deconvoluted XPS O1s peak of PGM-HEA (**Figure S4d**), further verifying the successful introduction of hydrophilic functionalities.

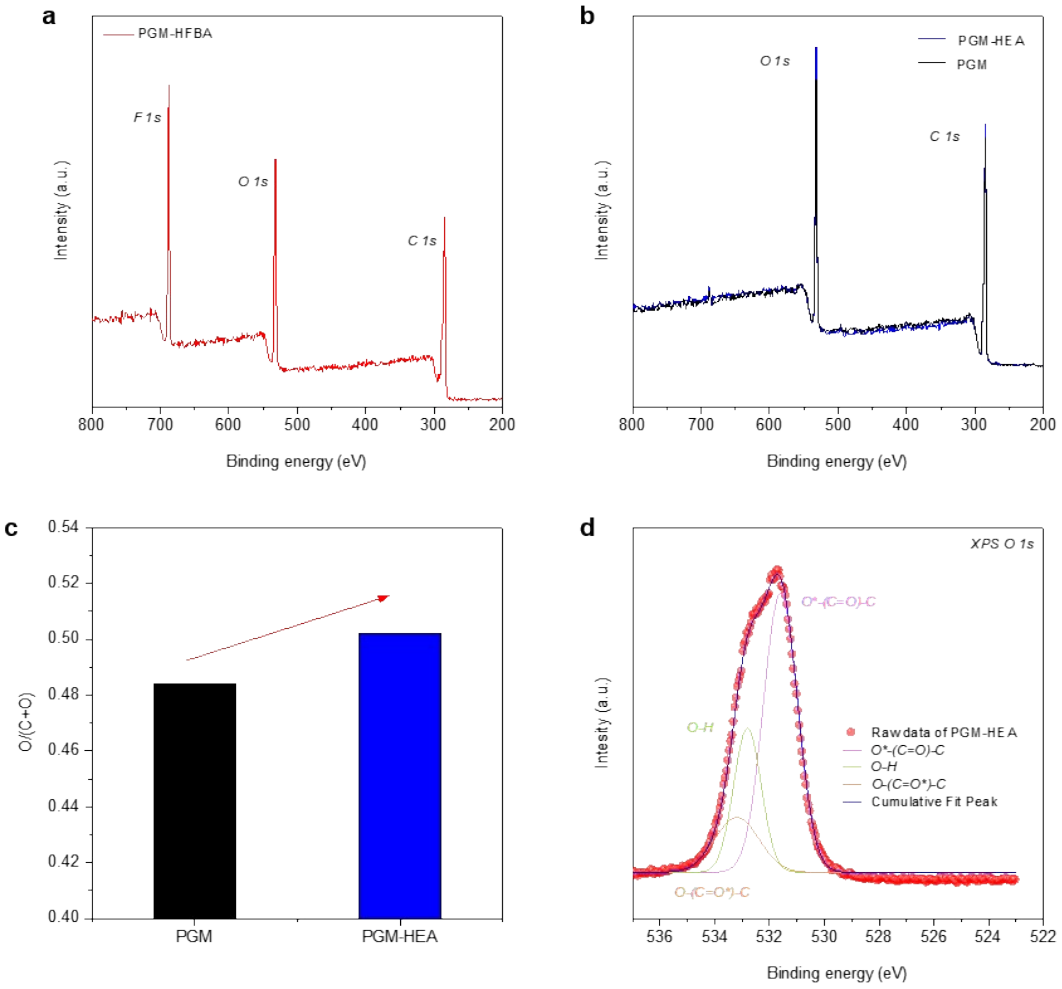

Figure S4. Surface XPS analysis of (a) PGM-HFBA, showing the presence of the fluorine 1s peak due to HFBA incorporation, (b) PGM (black line) and (c) PGM-HEA (blue line), illustrating the increased surface oxygen content in PGM-HEA compared to PGM. (d) Deconvoluted O 1s XPS spectrum of PGM-HEA, confirming the presence of O-H bonding, indicative of successful HEA integration.

Discussion on the optical performance of PGM film

Figure S5 presents the UV-visible spectroscopy analysis of the PGM transparent film. The film exhibits minimal light transmission in the UVA range but begins to transmit light in the transition from UVA to UVB. Notably, the film allows nearly 80% of visible light to pass starting from 400 nm, providing clear evidence of its high transparency. This result confirms the optical clarity of the PGM film, making it suitable for applications requiring transparent and functional polymeric materials.

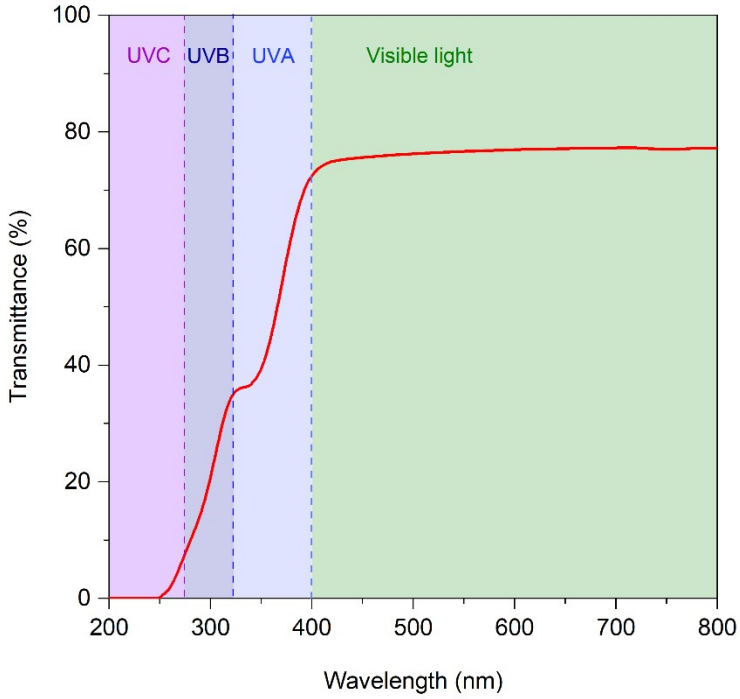

Figure S5. UV-visible spectroscopy of transparent PGM film.

Discussion on the NaCl removal from sponge

Figure S6 presents SEM and EDS images of the sponge after NaCl removal, verifying the effectiveness of the salt template removal process. As shown in **Figure S6a**, the SEM image reveals no significant presence of NaCl residues, indicating a well-cleansed porous structure. However, in **Figure S6b**, a few small NaCl particles were detected. These remaining particles were negligibly small and are unlikely to affect the structural or functional properties of the sponge, confirming the successful removal of the salt frame.

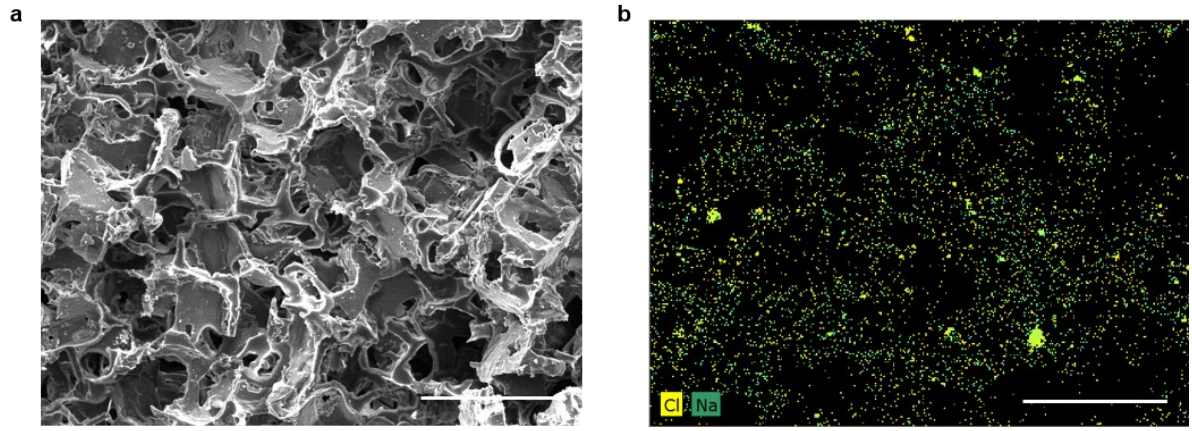

Figure S6. (a) SEM and (b) EDS images of NaCl removed sponge (scale bar = 300 μm).

Observation of pore size controllability

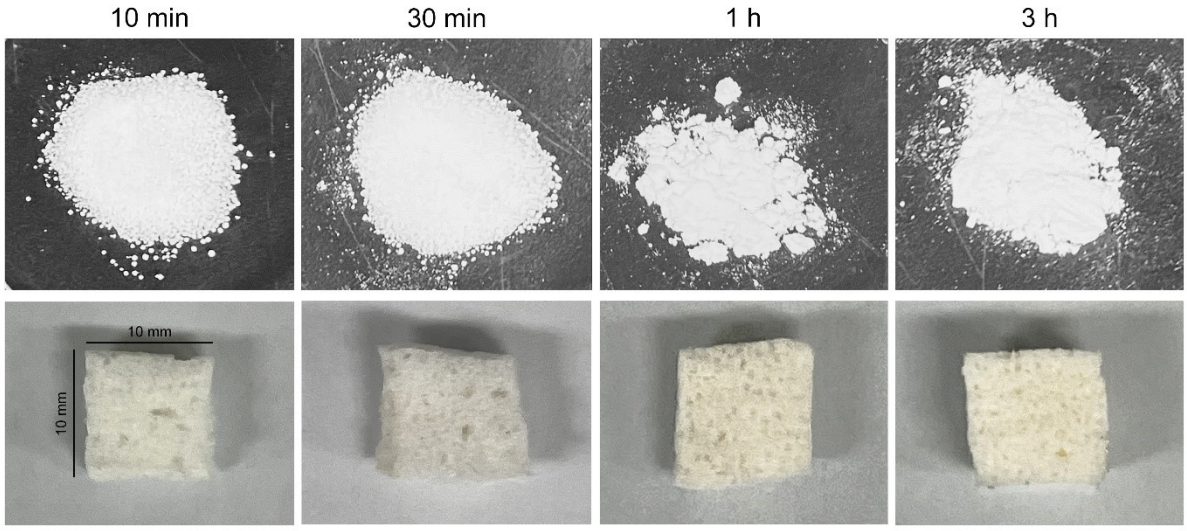

Figure S7. Photographs of NaCl particles (above) and sponges (below) according to the ball-milling time.

Discussion on the surface wetting behavior of PGM sponge

The surface behaviors of PGM film and PGM sponge are significantly different whether the pores exist or not. As described in Figure 1i and 2h, water contact angle values are different for PGM-HFBA, especially being much higher in the sponge state compared to the flat film state (almost 40° higher). This phenomenon can be interpreted using wetting models that describing the relationship between wetting properties and surface morphology. For example, in the case of the hydrophobic HFBA incorporated PGM-HFBA sponge, one possible explanation is the Cassie-Baxter model, in which the liquid droplet contacts both the solid surface and the trapped air within surface roughness. [7, 8] If the content of HFBA in the PGM-HFBA sponge increases, the hydrophobicity of the sponge skeleton is also enhanced, and the air layers of the pores can be better preserved, as illustrated in **Fig. S8a**. However, it should be noted that, while the Cassie-Baxter model is used to explain the behavior of the PGM-HFBA sponge, this is only one possible assumption and scenario. It was difficult to conclusively determine the exact wetting state, due to the experimental limitations. By contrast, the behavior of the PGM-HEA sponge is better explained by the Wenzel model. As the HEA concentration increases, the hydrophilicity of the sponge skeleton increases, enabling water penetration into the porous air gaps. Therefore, Wenzel model–assuming full wetting of the surface including the pore structure–might be more appropriate for explaining liquid contact behavior on PGM-HEA sponge (simply illustrated in **Fig. S8b)**. However, the precise wetting state (Cassie-Baxter vs. Wenzel) cannot be conclusively determined due to the complexity of the system and experimental limitations.

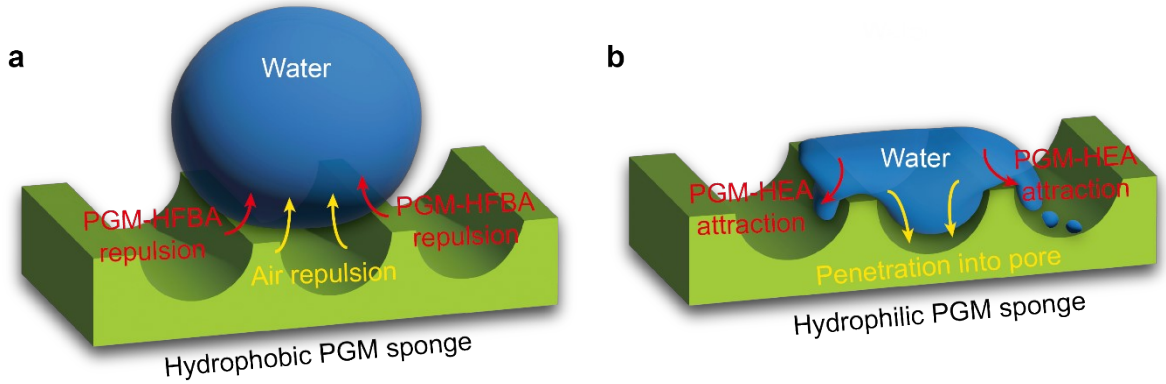

Figure S8. Illustration of water droplet contact on (a) hydrophobic PGM sponge, and (b) hydrophilic PGM sponge.

Observation of the PGM-HFBA sponge during oil/water separation process

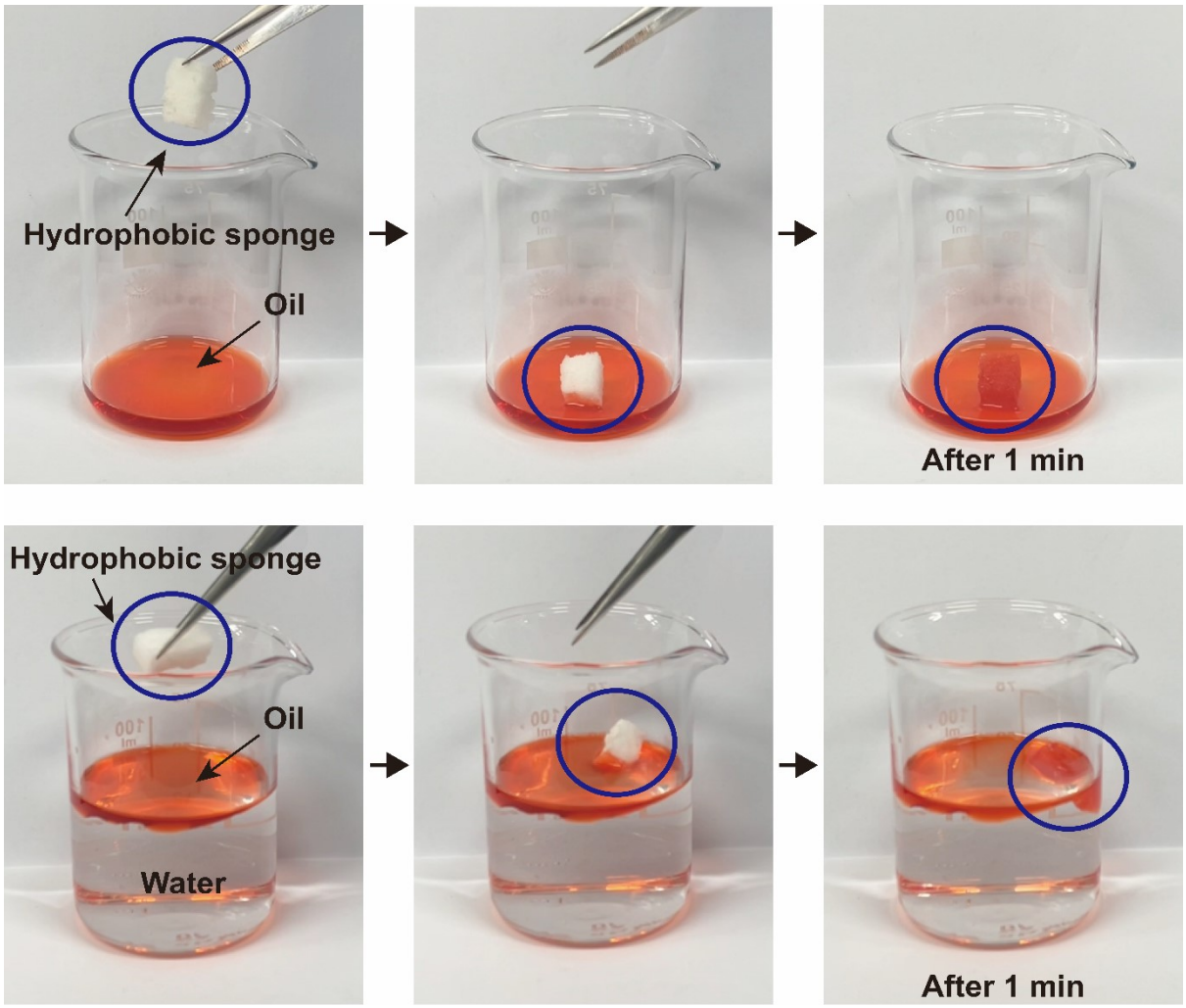

Figure S9. Photographs for the evaluation of oil absorption capacity (above) and separation efficiency (below).

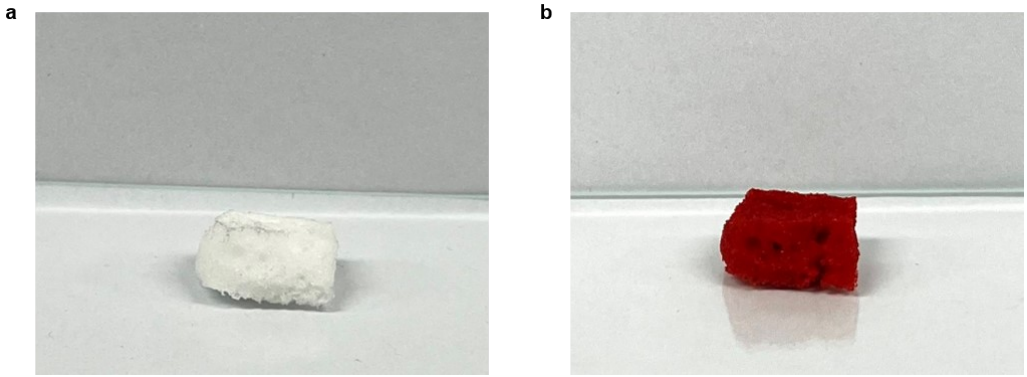

Figure S10. Photographs of the PGM-HFBA sponge (a) before oil absorption and (b) after 100 cycles of oil absorption, where the sponge appears red due to the presence of Oil Red dye in the silicone oil.

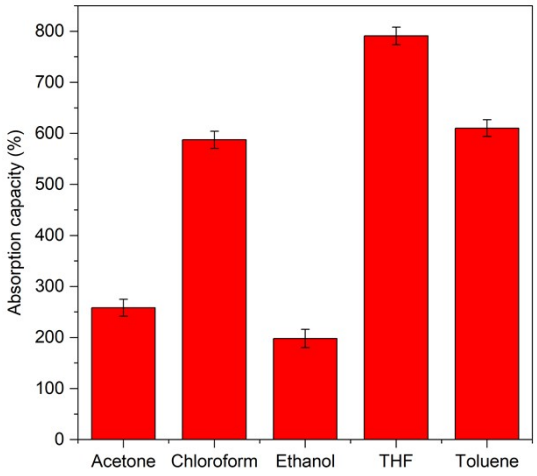

Figure S11. Absorption capacity of PGM-HFBA sponge for various organic solvents (error bars calculated based on measurements from more than 10 data points each).

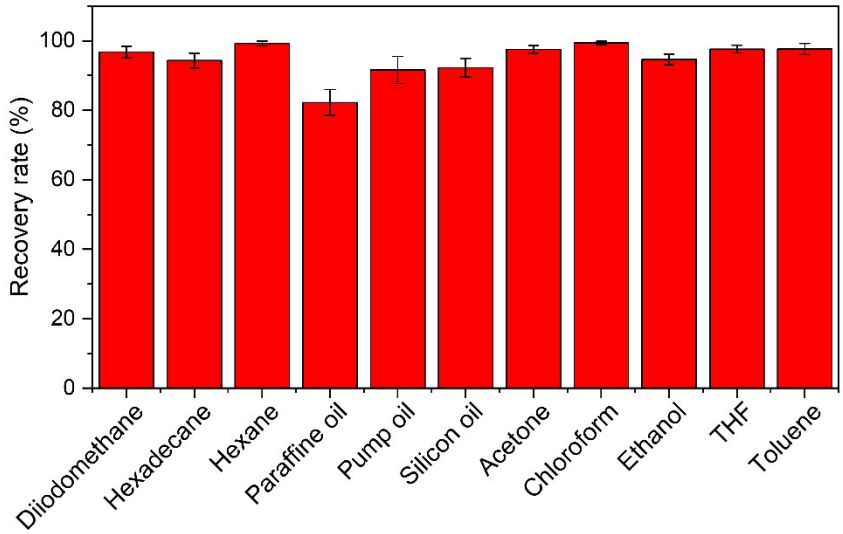

Figure S12. Oil/solvent recovery rate according to the liquid type.

Table S1. Absorption capacity of various oils calculated by absorbed oil volume per weigh of sponge.

Oil	Diiodomethane	Hexadecane	Hexane	Paraffine oil	Pump oil	Silicon oil
Aborption capacity (mL/g)	0.744	3.715	7.709	2.759	6.193	3.153

Table S2. Absorption capacity of various organic solvents calculated by absorbed solvent volume per weigh of sponge.

Organic solvent	Acetone	Chloroform	Ethanol	Tetrahydrofuran	Toluene
Aborption capacity (mL/g)	3.297	3.943	2.511	8.899	7.039

Table S3. Absorption capacity in our work compared with existing studies.

Used material	Oil/solvent type	Absorption capacity	[Ref]
Crosslinked polyacrylate	Hexane	509.29%	Our work
Crosslinked polyacrylate	Toluene	610.29%	Our work
Polyurethane	N-hexane	16.5%	[7]
Polyurethane	N-hexane	37.69%	[8]
Polyurethane	Hexane	375%	[9]
Polydimethylsiloxane	Toluene	445%	[10]
Polydimethylsiloxane	Toluene	≈400%	[11]

Discussion on liquid metal (LM) absorbed and pristine PGM-HEA sponges

The resistance of the LM-absorbed sponge was measured to evaluate its electrical conductivity using a digital multimeter (Hioki 3244-60) (**Figure S14**). The pristine PGM-HEA sponge exhibited extremely high resistance, exceeding the measurement limit, indicating its non-conductive nature. In contrast, the LM-absorbed PGM-HEA sponge demonstrated a significantly low resistance, approaching 0 Ω/cm, confirming its excellent electrical conductivity. These results indicate that the liquid metal was successfully infiltrated into the sponge matrix, forming continuous conductive pathways and effectively enhancing the electronic conductivity of the LM-absorbed PGM-HEA sponge.

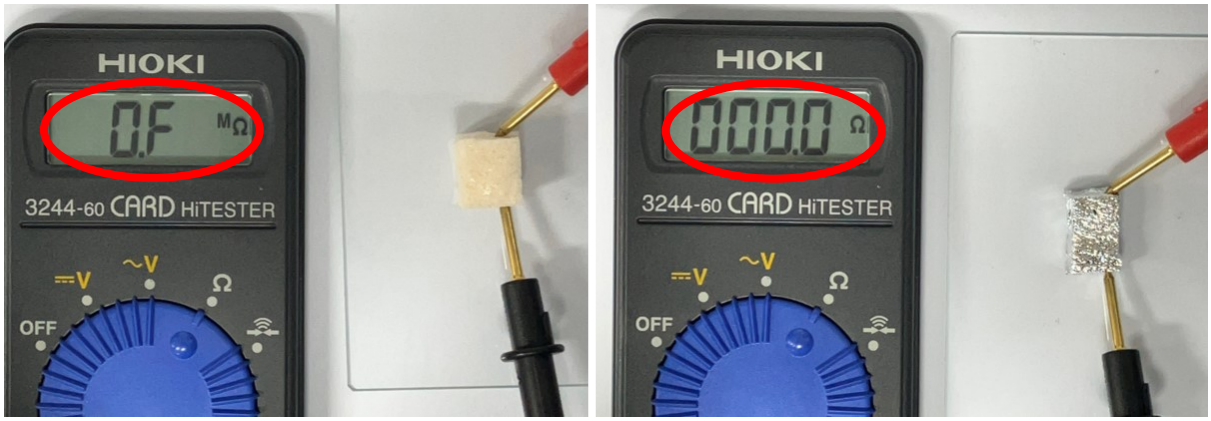

Figure S13. Measured resistance of pristine PGM-HEA sponge (left) and LM absorbed sponge (right) using an Ohmmeter

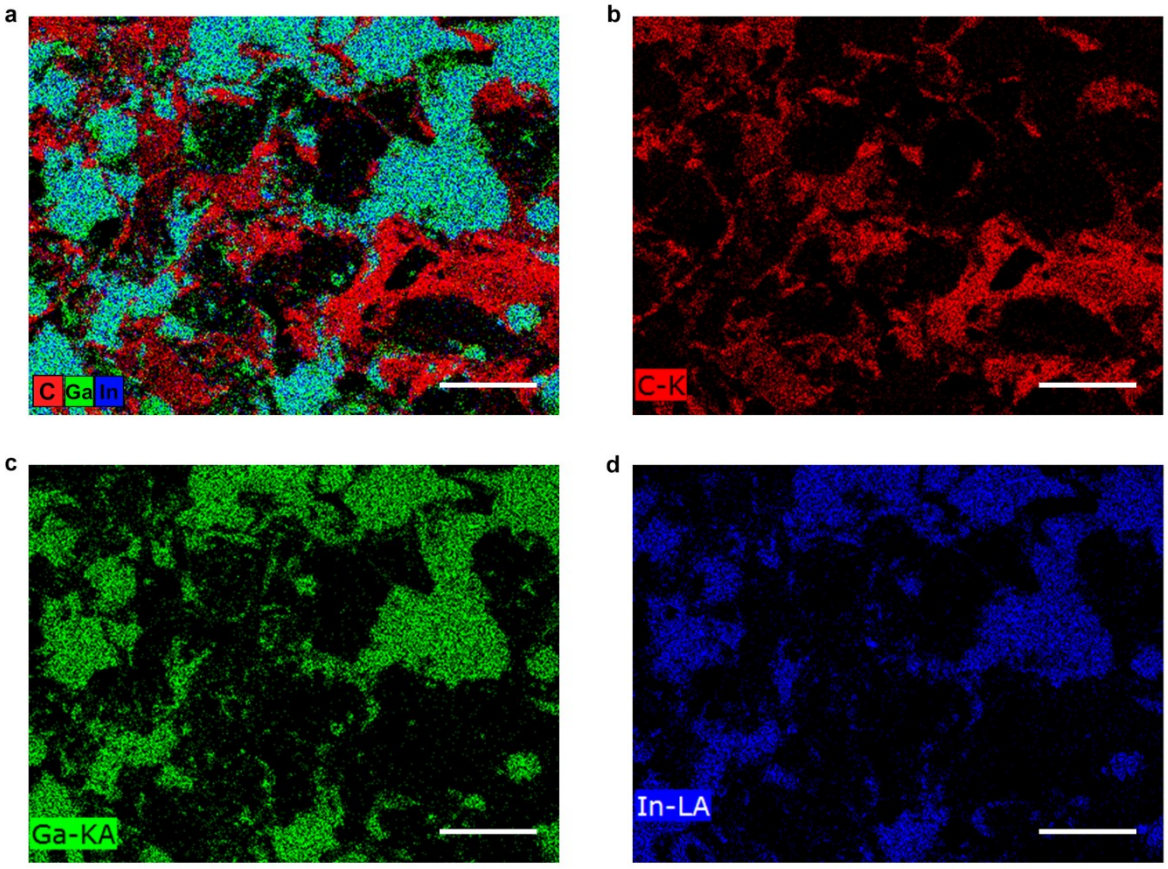

Figure S14. EDS mapping images of (a) all elements, (b) carbon, (c) galium, and (d) indium.

Discussion on comparison of PGM sponge and PDMS sponge

To demonstrate the superior elasticity of the PGM sponge, a PDMS sponge was prepared using Sylgard 184 following the same salt-frame templating method. As shown in **Figure S15**, the PDMS sponge exhibited an elongation at break of approximately 70%, which was significantly lower than that of the PGM sponge. Additionally, the PDMS sponge displayed higher maximum stress and Young's modulus, indicating that it is stiffer and requires greater energy for mechanical deformation compared to the PGM sponge.

These findings highlight the advantages of the PGM sponge, which offers enhanced elasticity and flexibility, making it more suitable for applications requiring highly stretchable and deformable porous materials. The superior mechanical properties of the PGM sponge further emphasize its potential as an advanced functional material compared to conventional elastomeric sponges such as PDMS.

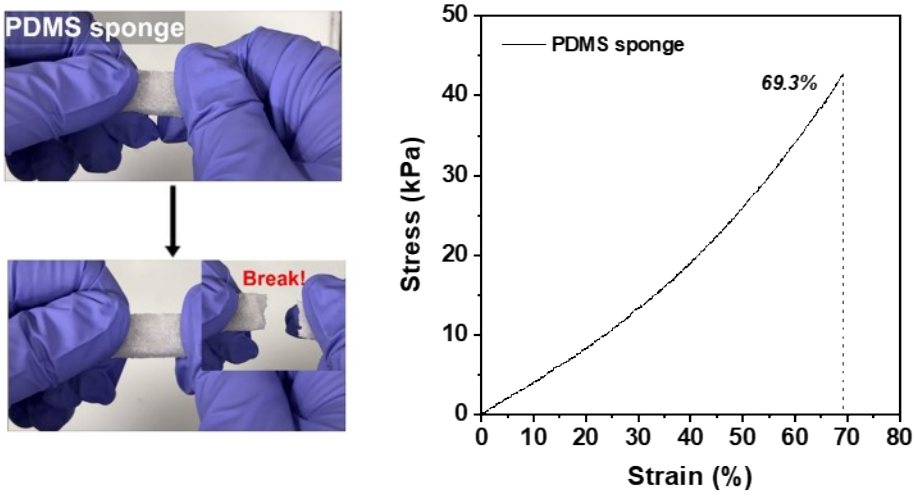

Figure S15. Photographs of stretched PDMS sponge (left) and strain-stress curve of PDMS sponge (right).

Table S4. Detailed mechanical information of PDMS sponge.

	Elongation at break (%)	Maximum stress (kPa)	Young`s modulus (kPa)	Toughness (kPa)
PDMS sponge	69.3	43	47	12

Moreover, we attempted to infiltrate the same liquid metal into the PDMS sponge under identical conditions as those used for the PGM-HEA sponge. However, even in SEM and EDS images of the cross-section (**Figure S16**), no significant liquid metal penetration was observed. This limitation arises due to the inherently superhydrophobic nature of the PDMS sponge, which restricts the infiltration of liquid metal into its internal structure. Furthermore, modifying the wettability of PDMS to achieve hydrophilicity typically requires additional surface treatments, such as plasma exposure or the introduction of surface-modifying particles.[9, 10]

In contrast, the PGM-based sponge demonstrated a significant advantage in its ability to freely and precisely control surface wettability, allowing seamless liquid metal penetration. This tunable wettability feature, which is challenging to achieve with conventional materials like PDMS, highlights the superior adaptability and functional versatility of the PGM sponge for advanced applications.

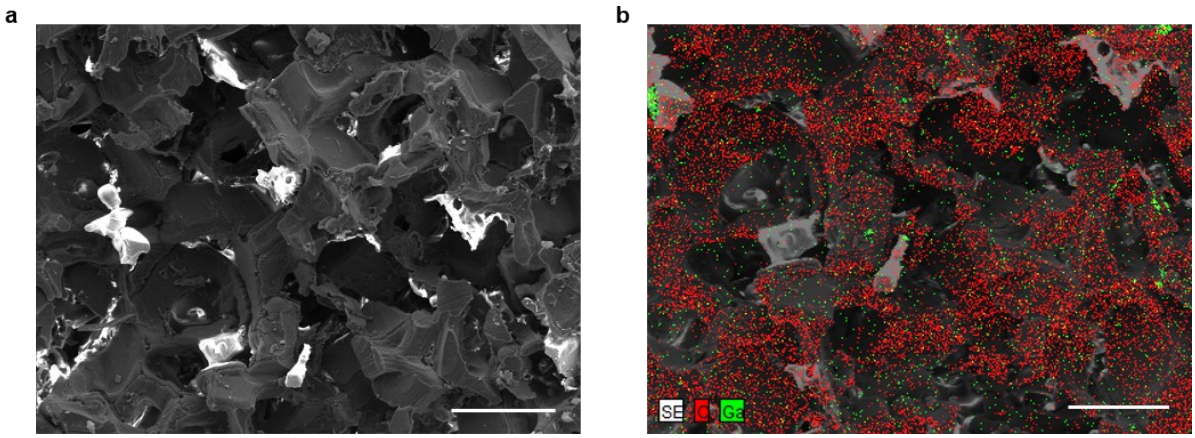

Figure S16. (a) SEM and (b) EDS images of LM absorbed PDMS sponge (scale bar = 300 μm).

References

1. Kaelble, D., *Dispersion-polar surface tension properties of organic solids.* The Journal of Adhesion, 1970. **2**(2): p. 66-81.
2. Owens, D.K. and R. Wendt, *Estimation of the surface free energy of polymers.* Journal of applied polymer science, 1969. **13**(8): p. 1741-1747.
3. Rabel, W., *Einige Aspekte der Benetzungstheorie und ihre Anwendung auf die Untersuchung und Veränderung der Oberflächeneigenschaften von Polymeren.* Farbe und Lack, 1971. **77**(10): p. 997-1005.
4. Holmberg, K., *Handbook of applied surface and colloid chemistry.* (No Title), 2002.
5. Birdi, K., *Handbook of surface and colloid chemistry*. 2008: CRC press.
6. Bermejo, J.S. and C.M. Ugarte, *Influence of cross-linking density on the glass transition and structure of chemically cross-linked PVA: a molecular dynamics study.* Macromolecular theory and simulations, 2009. **18**(6): p. 317-327.
7. Giacomello, A., et al., *Metastable Wetting on Superhydrophobic Surfaces: Continuum and Atomistic Views<? format?> of the Cassie-Baxter–Wenzel Transition.* Physical review letters, 2012. **109**(22): p. 226102.
8. McHale, G., *Cassie and Wenzel: were they really so wrong?* Langmuir, 2007. **23**(15): p. 8200-8205.
9. Zhou, T., et al., *Hydrophilic sponges for leaf-inspired continuous pumping of liquids.* Advanced Science, 2017. **4**(6): p. 1700028.
10. Chen, I.-J. and E. Lindner, *The stability of radio-frequency plasma-treated polydimethylsiloxane surfaces.* Langmuir, 2007. **23**(6): p. 3118-3122.